© 2023 IEEE

Power Electronics and Applications (EPE'23 ECCE-Europe), 2023 25th European Conference on

Thermal Design of a Medium Voltage Modular Multilevel Converter Cell

Y. Frei and D. Dujic

This material is posted here with permission of the IEEE. Such permission of the IEEE does not in any way imply IEEE endorsement of any of EPFL's products or services. Internal or personal use of this material is permitted. However, permission to reprint / republish this material for advertising or promotional purposes or for creating new collective works for resale or redistribution must be obtained from the IEEE by writing to pubs-permissions@ieee.org. By choosing to view this document, you agree to all provisions of the copyright laws protecting it.

POWER ELECTRONICS LABORATORY
ÉCOLE POLYTECHNIQUE FÉDÉRALE DE LAUSANNE

Thermal Design of a Medium Voltage Modular Multilevel Converter Cell

Yanick Patrick Frei, Drazen Dujic
Power Electronics Laboratory, École Polytechnique Fédérale de Lausanne (EPFL)
CH-1015 Lausanne, Switzerland
E-Mail: yanick.frei@epfl.ch, drazen.dujic@epfl.ch
URL: https://www.epfl.ch/labs/pel/

***Index Terms*—Modular Multilevel Converters (MMC), Thermal design.**

***Abstract*—This paper presents the cooling concept for a medium voltage modular multilevel converter cell. To optimize power density, the metallic enclosure is used to dissipate the heat generated by semiconductor losses, while maintaining maximum temperatures below desired levels. Design, simulation results, and several different prototypes are verified and validated experimentally for their performance.**

I. Introduction

For medium voltage converters, the Modular Multilevel Converter (MMC) is an interesting topology thanks to its comparably low voltage ratings of the devices in the series-connected cells or submodules, superior harmonic performance, scalability, and redundancy [1]. While the classic MMC, used for HVDC applications, converts AC to DC and vice versa, the Direct-MMC (D-MMC or M3C), presented first in [2], offers a direct connection between two AC grids using a matrix-like structure, c.f. Fig. 1. Due to the working principle of the D-MMC, requiring balanced energies within the branches, operation with similar or identical frequencies at the two AC ports is typically avoided [3]. An additional difference between the classic MMC and the D-MMC is the need to generate negative branch voltages, thus full-bridge cells are required.

Hydropower applications, in order to improve their operational flexibility, are being increasingly retrofitted with VSCs. In particular, pumped hydro storage plants have to be able to adjust their power quickly, including the transition from pumping to turbine mode and vice versa [4]. This can be achieved with variable speed operation, which also increases efficiency. Allowing for a variable speed operation of medium voltage machines with full torque from zero speed [4], the D-MMC is perfectly suitable for hydropower applications. A first installation with two 80 MW 18 kV synchronous machines has been commissioned in 2021 in Galgenbichl, Austria [5]. This is the main application motivating the work presented in this paper.

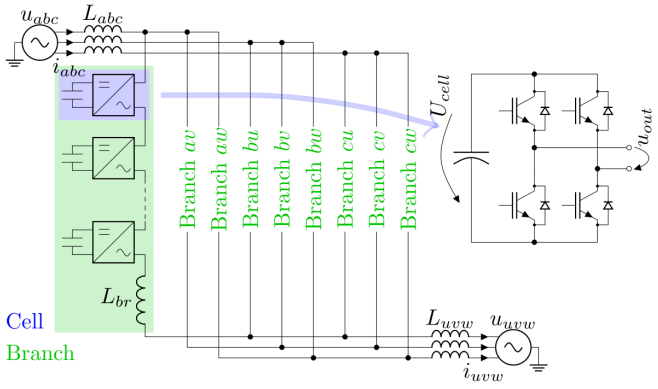

Fig. 1. Structure of the Direct-MMC. Only one branch is shown in detail with full-bridge series-connected cells and branch inductance.

Besides the semiconductors, each cell has an energy storage in the form of a capacitor. Due to the working principle of the MMC, it is usually rather big and voluminous compared to other converter topologies. In case of a fault within a cell, protection equipment bypasses the cell and the MMC offers the possibility to continue operation with redundant modules after reconfiguration. The protection scheme is implemented differently based on the type of semiconductors. Presspack devices for MMC cells have robust diodes which typically survive the destruction of the switch, hence protection is implemented by a thyristor crowbar in the DC-link. With plastic module packages, diodes are typically much weaker, and each cell is protected individually with a bypass on the AC terminals of the cell.

Commercial MMCs are mainly IGBT based [6]–[8],

while recently IGCT-based MMCs for hydropower, rail interties, and STATCOM for medium voltage applications have been launched on the market [9]. Besides Silicon based MOSFET and IGBT solutions, SiC MOSFET-based academic MMC prototypes can be found as well [10]–[14]. Their designs are motivated by higher blocking voltages and switching frequencies of the semiconductors, as well as by higher integration possibilities thanks to higher operating temperatures and lower power losses.

Clearly, the MMC is an attractive research topic. Many research laboratories have their own small-scale prototypes, which are often used for control development with minor efforts invested towards hardware design optimization. They are often rated for low power and without the need for thermal design provisions. There are, however, many academic prototypes with significant ratings, such as [10], [13]–[22].

Almost all reported MMC designs use either natural or forced air cooling, or water cooling for their cells. Some exotic proposals also can be found, such as the use of a vapor chamber in [12]. Offering a good trade-off between cooling capabilities, volume and complexity, forced convection is the dominant solution and all of the above-mentioned academic prototypes [10], [13]–[22] rely on forced convection and are often not enclosed in cabinets, but realized as open-frame designs.

In [13], the authors present a detailed thermal analysis for the realized MMC prototype. Each cell is equipped with its own fan, attached directly to the heatsink, on which the power module is installed, greatly simplifying the overall design. However, the semiconductors are taken as the only heat source on a cell level.

A more detailed thermal modeling study has been presented in [15], where the Foster network is extended to include several heat sources influencing each other. In addition to the semiconductors, which are on a cell level installed on the same heatsink, also capacitors and bleeding resistors are included. Next to the steady-state temperature analysis, the transient behavior is investigated as well. This is done by FEM simulations first on the cell level and later on, using a simplified cell model, over the whole converter. Modeling results are verified on an experimental setup of a $15\,\mathrm{kVA}$ converter with 18 cells, IGBT-based, with a nominal cell voltage of $900\,\mathrm{V}$. The converter setup is realized as an open frame with forced convection for cooling.

Another detailed thermal simulation study is done in [14], using $10\,\mathrm{kV}$ SiC semiconductors. The analysis is provided considering forced air conditions for the heatsink of the cell, including the losses of the semiconductors and the bleeding resistors. On a converter level, different arrangements of cabinet fans (in addition to the cell-level fans) are compared to remove heat while at the same time offering uniformal temperature distribution. This is best achieved by having suction fans installed on the side of the cabinet. However, this has also been the only studied setup using multiple fans, obstructing the general validity of the statement, as it is unclear to which extent the improvement comes from the airflow direction or the increased quantity. Furthermore, experimental results are omitted.

The work presented in this paper considers a cabinet-enclosed MMC design with forced air cooling at the cabinet level. Yet, the results presented in the paper are related to the thermal design of the cell, where a metallic enclosure is used to remove the semiconductor losses. Detailed analysis, modeling, thermal simulations and verifications are presented, confirming the validity of the presented concept.

II. Cell Design

In previous works [19], a $250\,\mathrm{kVA}$ MMC rated for $\pm 5\,\mathrm{kV}$ on the DC side and $3.3\,\mathrm{kV}$ on the AC side has been developed. It consists of eight cells per branch (48 in total), of which one is shown in Fig. 2. The $1.2\,\mathrm{kV}$ IGBT module, mounted on the visible heatsink, together with the cell capacitors are forming the high-power part of the cell. A second low-power PCB is added on top, hosting e.g. the processor, gate drivers and auxiliary power supply. Cooling is done by forced airflow through the cell, realized by multiple fans mounted on the cabinet's back side walls.

This converter layout and control system [23] serves as a base for the $6.0/6.6\,\mathrm{kV}$, $600\,\mathrm{kVA}$ D-MMC prototype under development. To preserve the existing control system and communication protocols, the number of cells per branch is kept the same. With this in mind, the ratings of the new HV cell are derived and shown,

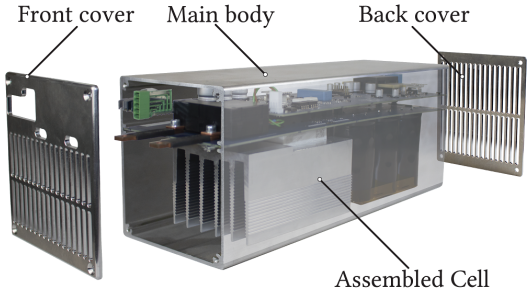

Fig. 2. The low voltage MMC cell installed in the metallic enclosure.

TABLE I
RATINGS OF THE TWO MMC CELLS.

Property	LV cell	HV cell
Max. cell voltage $\hat{U}_{cell}$	900 V	2000 V
Semiconductor voltage class	1.2 kV	3 kV
Branch rms current I_{br}	50 A	25 A
Cell capacitance C_{cell}	2.25 mF	0.8 mF
Stored cell energy E_{cell}	911.25 J	1600 J
Cell switching frequency $f_{sw,cell}$	1 kHz	1 to 10 kHz
Enclosure size $l_b \times w_b \times h_b$	$325 \times 110 \times 125$ mm	

for comparison, together with the ratings of the LV cell in Table I.

The higher cell voltage of 2 kV requires new semiconductors, in this case, 3 kV discrete IGBTs with a current rating of 34 A are chosen. Keeping the control system identical, switching frequencies from 1 kHz to 10 kHz are considered during thermal design. The HV cell capacitance requirements are derived as 800 µF and realized as four strings of five series-connected 450 V, 1.0 mF capacitors.

The interior volume of the cell enclosure is around 4.5 l and in the LV cell design, the capacitor bank occupies 14 % of it, while in the HV cell, the needed volume represents 26 %, leaving little space for a commercial heatsink for the power semiconductors. This is why the possibility to use the metallic enclosure to dissipate the losses is investigated. Another reason for this is the fact that the semiconductor losses are reduced in the HV cell (presented in the next section) in comparison to the LV cell [19].

The ISOPLUS i4 (similar to TO-264) package of the semiconductors comes with an isolated tab, removing the need for electric isolation towards the enclosure. In the design, the cell enclosure is on the negative potential of the internal DC link, which defines the local maximum voltage for the insulation coordination inside the enclosure [24]. However, the clearance distance from the device pins to the enclosure has to be regarded. To provide sufficient distance for clearance while at the same time improving the thermal performance by offering a greater cross-section for the heat flow than the 2.5 mm thick enclosure, a heat spreader is designed between the devices and the enclosure. The set maximum allowed temperature of the junction is 125 °C, while the enclosure has to stay below 60 °C, both with an ambient temperature of 40 °C. The latter constraint should avoid the other interior electronic components of the cell being exposed to excessive thermal stress.

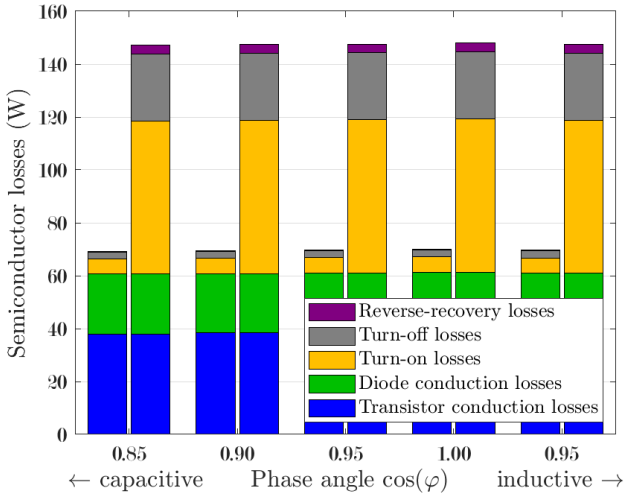

Fig. 3. Total semiconductor losses for different phase angles for one AC side, while the other is kept at 0°; the left bar is with a switching frequency of 1 kHz, the right one with 10 kHz.

III. THERMAL DESIGN

To determine the worst-case semiconductor losses, simulations are performed, taking into account the relevant operating conditions. The semiconductor devices considered for the design are IXBF55N300 by IXYS with a thermal resistance between junction and the case of 0.5 K W^{-1}, and operation with switching frequencies between 1 kHz and 10 kHz has been simulated. Results for the two extreme cases are shown in Fig. 3, where with 1 kHz, conduction losses are the dominant part of the total 70 W losses of all devices; operation at 10 kHz leads to the same conduction losses, but higher switching losses, resulting in a total of around 150 W. To ensure some thermal margin in the design, total losses of 200 W (or 50 W per device) are considered for thermal simulations and evaluation of thermal performances of different heat spreader geometries. The total losses are equally split between the two HV cell legs.

The semiconductors are paired, forming half-bridge legs of the cell, and installed close to the inlet of the enclosure on each side wall. This position is not only advantageous in a thermal way, as the cooling air is with the lowest temperature, but also given by electric constraints: clearance and creepage towards the enclosure, with the only free parameter being the distance to the enclosure. This defines the thickness of the heat spreader, t_{hs} in Fig. 4. Similarly, additional constraints for the heat spreader geometry can be defined:

- due to the isolation of the package, a minimum distance from the wall is given, which can be further

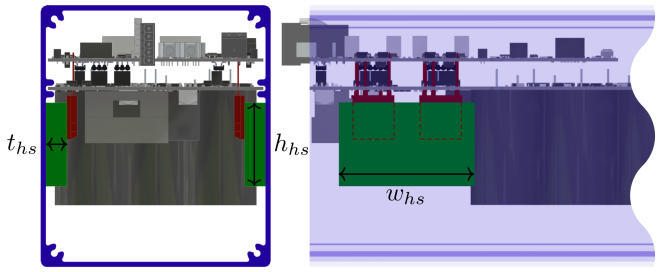

Fig. 4. Positioning of the heat spreader (green) with the semiconductors (red) within the enclosure (blue).

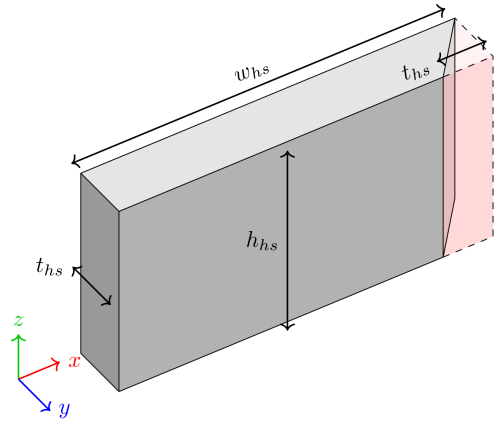

Fig. 5. Geometrical definition of the simulated heat spreaders with the red volume being removed by optional chambering.

increased;
- height is restricted by the internal mechanical design and details of the enclosure;
- length is restricted by the need to leave room for other components such as the capacitor bank.

The resulting constraints for a heat spreader geometry according to Fig. 5 are summarized as numerical values in Table II. Thanks to its good thermal conductivity, simple processing, and the absence of corrosion, the material of the heat spreader has been chosen to be identical to the enclosure, namely aluminium.

As the amount of air flowing through the interior of the cell is unknown at this stage, the cooling mainly relies on the airflow around the cell. This stands in contrast to the LV cell [19], where the thermal management is done relying completely on the internal airflow.

TABLE II
MECHANICAL CONSTRAINTS OF THE HEAT SPREADER.

Property	Range
Heat spreader width w_{hs}	49.8 mm to 90 mm
Heat spreader height h_{hs}	15.6 mm to 71.9 mm
Heat spreader thickness t_{hs}	11.2 mm to 18 mm

IV. THERMAL SIMULATIONS

To have an idea about the performance of the heat spreader, thermal simulations have been performed using COMSOL. As in the real cell airflow will be partially blocked by the front and back cover as well as by electronic components of the cell, two simulations with completely open and completely closed enclosures have been performed, being the two extreme cases.

The heat spreader width is fixed as $w_{hs} = 90\,\mathrm{mm}$, being also chambered at the back. From the remaining two-dimensional design space, the heat spreader thickness has been simulated as 12, 15 and 18 mm, while height has been considered with steps of 10 mm from 30 mm to 70 mm.

According to the requirements, 200 W of total losses are assumed (which means 50 W generated per device and 100 W passing through each heat spreader), with the ambient temperature being set to the maximum expected of 40 °C. Between the heat spreader and the enclosure as well as the semiconductors, a layer of thermal grease ($r_{th} = 0.333\,\mathrm{K\,m\,W^{-1}}$) with a thickness of 0.2 mm is added. The reported airflow is the average over the 0.29 m side length squared cross-section considered centered around the enclosure. Besides the semiconductors, the heat spreaders, and the enclosure, no further components of the cell have been modeled.

The impact of geometry is presented in Fig. 6, where the change due to the heat spreader length and thickness can be seen. The first observation is that the enclosure hotspot temperature is clearly the more critical one, while the junction temperature is below the prescribed limits. In the case of the fully opened enclosure, cooling capabilities are improved, as the surface on which heat can be dissipated directly to the ambient air is greatly increased. This allows a small amount of heat to be dissipated directly from the source to the air, whereas another (greater) part flows through the heat spreader, from where it is dissipated directly to the cooling air. Another obvious improvement can be seen when using a thicker and longer heat spreader. The latter increases the area in contact with the enclosure, making not only the area of the comparably bad (with respect to aluminium) thermal grease bigger but also increasing the area within which good heat conduction along the enclosure surface can be offered. A starting saturation effect can however be seen at the maximum of the investigated height. A thicker heat spreader will allow for a more homogeneous temperature profile within the heat spreader.

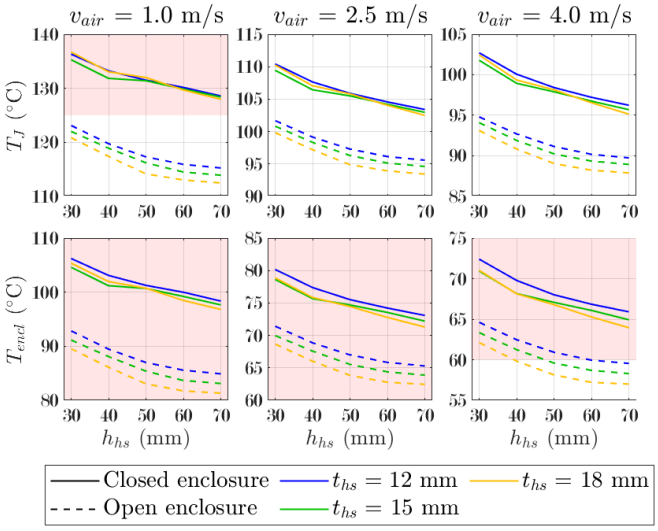

Fig. 6. Estimated temperatures of interest for different heat spreader geometries.

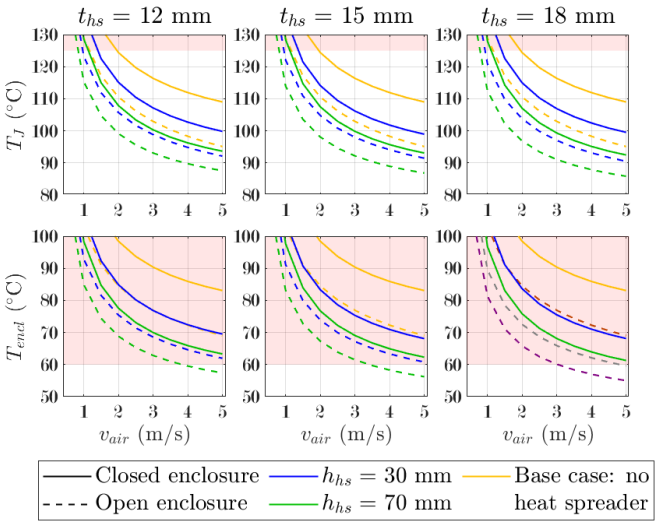

Fig. 7. Estimated temperatures for different cooling air speeds (only the heights 30 mm and 70 mm are shown for the sake of clarity).

Fig. 7 shows the results for the different heat spreader geometries with different temperatures. In this figure, also the base case with no heat spreader is introduced for comparison, revealing the clear improvements achieved with the heat spreaders. With all geometries, cooling air speeds of at least $3\,\mathrm{m\,s^{-1}}$ are required.

In Fig. 8, the temperature profile is exemplary shown for one simulation. It reveals that indeed only the part of the enclosure close to the heat spreader has a significant temperature difference towards the ambient and thus participates in the cooling effort or, in other words, enables heat flow to the cooling air. Along the y-axis,

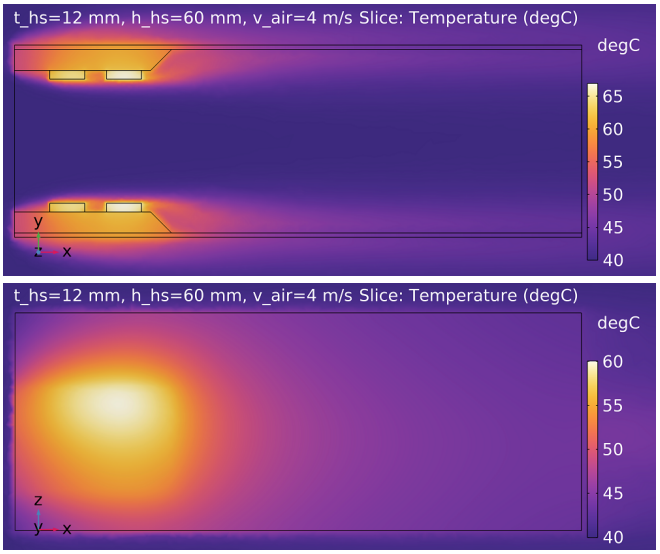

Fig. 8. Temperature distribution of a cut at the middle of the semiconductor height (top) and on the side of the enclosure (bottom).

no major temperature drop occurs, whereas orthogonal to that, a clear temperature decrease can be seen when going away from the heat source.

V. Experimental Verification

To validate the selected heat spreader designs, a thermal setup, c.f. Fig. 9, has been designed. It consists of a wooden tunnel of $1.4\,\mathrm{m}$ length and a cross-section of $290\,\mathrm{mm} \times 290\,\mathrm{mm}$ with a removable Plexiglas cover. Incoming air is heated up, with the temperature being controlled in a closed loop. Temperatures are measured before and after the device under test (MMC cell enclosure with different heat spreaders) by four thermocouples and then averaging their readings. An adjustable speed fan is used to extract the air, whose flow is made as laminar as possible using a honeycomb frame. It can produce speeds of up to $5\,\mathrm{m\,s^{-1}}$. Before the experiment and for the fan speed calibration, internal air speed has been measured with a Pitot tube, which is removed during the experiment and therefore not shown in Fig. 9.

From the possible heat spreader geometries investigated in the previous section, four designs have been selected and prototyped for experimental investigation and are shown in Fig 10. They are named model A to D. For simplicity, cost reasons, and the large number of tests, instead of the actual semiconductors, selected matching resistors in a TO-247 package have been used as heat sources. The dimensions of the prototyped heat spreaders are:

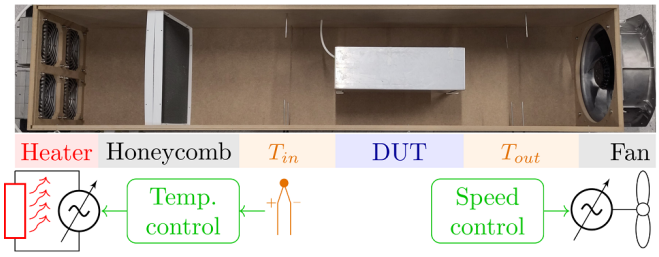

Fig. 9. The wind tunnel used for experimental verification (thermocouples within the cell are neither shown in the photo, nor in the description to avoid clutter).

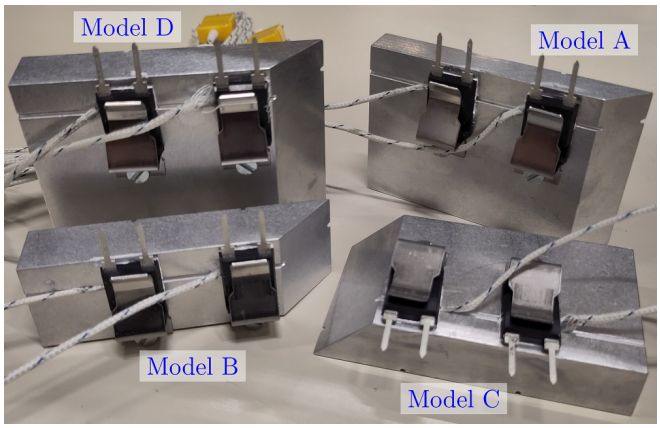

Fig. 10. Heat spreader designs with the heating resistors and thermocouples installed.

A: $t_{hs} = 12\,\mathrm{mm},\ h_{hs} = 60\,\mathrm{mm},\ w_{hs} = 90\,\mathrm{mm}$;
B: $t_{hs} = 18\,\mathrm{mm},\ h_{hs} = 30\,\mathrm{mm},\ w_{hs} = 90\,\mathrm{mm}$;
C: $t_{hs} = 18\,\mathrm{mm},\ h_{hs} = 50\,\mathrm{mm},\ w_{hs} = 90\,\mathrm{mm}$;
D: $t_{hs} = 18\,\mathrm{mm},\ h_{hs} = 70\,\mathrm{mm},\ w_{hs} = 90\,\mathrm{mm}$.

Grooves are milled to allow for the installation of thermocouples to measure the temperatures on both of their sides: between the heat spreader and the case of the device, and between the heat spreader and the enclosure. From the case temperature, one can calculate the junction temperature of the real semiconductor. To reduce possible measurement errors, all relevant positions are measured identically on both sides of the enclosure, as identical or very close readings were expected.

The position of the thermocouples and the temperature evolution (in the form of an exemplary set of data to illustrate the thermal dynamics of the system) in time is shown in Fig. 11, where the experiment has been started at room temperature and steady-state is reached after roughly half an hour. Air temperature changes only slightly from inlet to outlet, which is due to a large amount of air passing through the wind tunnel. The back measurement (the second one with respect to the airflow)

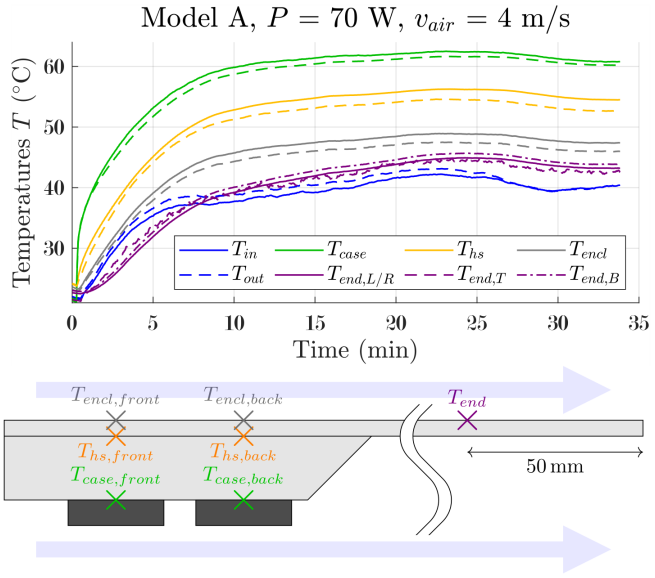

Fig. 11. Evolution of the measured temperatures with their location. Unless otherwise noted, dashed lines represent the front measurement, whereas the solid lines represent the back measurement point; L/R, T, and B represent the left/right average, top and bottom (located 50 mm away from the end of the enclosure, in the middle of the corresponding side).

is always slightly warmer than the front one, which can be easily explained by the thermal stacking effect. The temperature profile across the heat spreader ($T_{case} - T_{hs}$) is comparably big with respect to the one through the enclosure (perpendicular to the wall, $T_{hs} - T_{encl}$), due to the heat spreader being much thicker than the enclosure, with the latter in direct contact to the cooling medium (which might also affect the measurement). The temperature at the end of the enclosure is only slightly above ambient temperature, offering a safe environment for cell electronics.

The performance of the four different heat spreaders is compared in Fig. 12, with only average temperatures in steady-state being shown, resulting from the losses injected as presented in Fig. 3 as well as the design goal of 200 W. From there, a comparison can be done, c.f. Fig. 13, which confirms that all tested heat spreaders perform significantly better than the base case with the heat source installed directly on the enclosure.

The figures reveal that dissipating 150 W or even 200 W without exceeding the temperature limit of the enclosure is hardly feasible with the planned cooling effort. With losses of 70 W, expected with a switching frequency of 1 kHz, the goal can be fulfilled even at low cooling air speeds; above $2\,\mathrm{m\,s^{-1}}$ only minor improvements can be seen. Aiming for the removal of 200 W

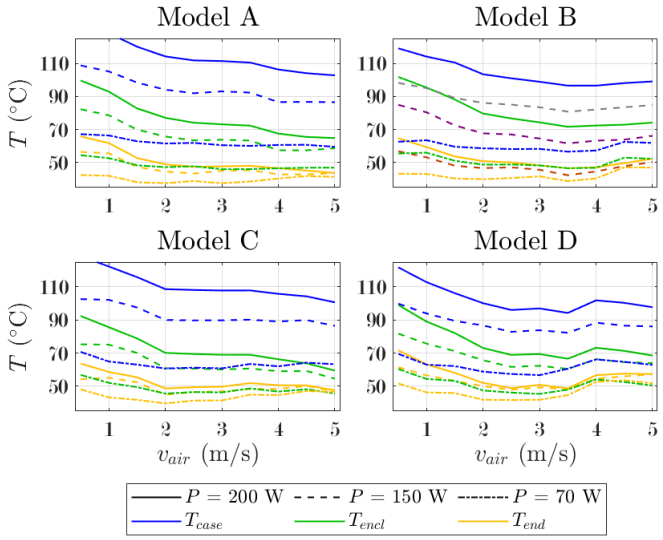

Fig. 12. Temperature of the different heat spreaders individually with varying power.

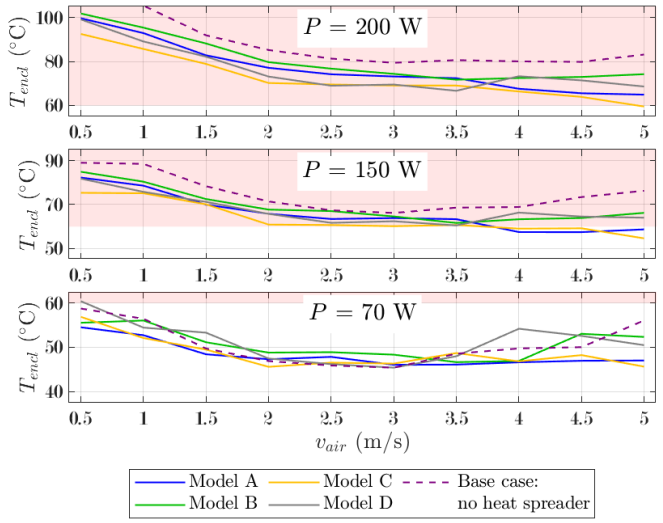

Fig. 13. Direct comparison of the heat spreader designs, the base case without heat spreader is added as well.

of losses, a better performing and thus geometrically larger heat spreader would be required. This, however, contradicts the original idea of the heat spreader, which is to allow as much space as possible for the capacitors. Approaches including a modification of the enclosure are disregarded, as this would as well penalize the original intention of the heat spreader investigation.

Looking at the end of the enclosure, except for very low cooling air speeds and high losses, the temperature always stays close to the ambient temperature, not exceeding $50\,^{\circ}\mathrm{C}$. In other cases, also the enclosure temperature behind the heat sources exceeds its limit.

The heat spreaders with a larger geometry perform better, as foreseen by the simulation. However, from model C to model D (increasing h_{hs} from $50\,\mathrm{mm}$ to $70\,\mathrm{mm}$), only a minor improvement can be seen. Being the least high one, model B ($h_{hs} = 30\,\mathrm{mm}$) shows the worst performance. The impact of thickness can also be observed, as model A has a height between models C and D, but a lower thickness ($12\,\mathrm{mm}$ compared to $18\,\mathrm{mm}$), performs not as good as these two. Still, a clear improvement compared to the situation without any heat spreader can be observed.

From the tested geometries, model A ($t_{hs} = 12\,\mathrm{mm}$, $h_{hs} = 60\,\mathrm{mm}$) has been selected for the final design. It shows satisfactory performances while keeping both the semiconductor and the enclosure temperature below their corresponding set limits. Being thinner than the other ones while still offering sufficient clearance distance, it leaves more space on the PCB, whose size is limited by the enclosure (c.f. Table I).

VI. Conclusion

This work presented the thermal considerations for a medium voltage MMC cell, including experimental validation. To increase power density, the metallic enclosure has been integrated into the thermal design with the goal to remove semiconductor losses. Different heat spreader geometries, allowing for better thermal contact between the semiconductors and the enclosure, have been analyzed while exposed to different semiconductor losses and cooling air speeds, deriving the needs of the converter cooling system to be developed at a later stage. Starting by exploring the design space of possible heat spreader geometries by means of FEM simulations, four of them have been experimentally investigated. The selected design with a thickness of $12\,\mathrm{mm}$, a height of $60\,\mathrm{mm}$ and a width of $90\,\mathrm{mm}$ (model A) consumes little space, while still keeping the temperatures below the set limits. Namely, the enclosure temperature can be kept below $60\,^{\circ}\mathrm{C}$ with an ambient temperature of $40\,^{\circ}\mathrm{C}$ with the assumed maximum losses of $150\,\mathrm{W}$ appearing at a switching frequency of $10\,\mathrm{kHz}$ and a cooling air speed of $4\,\mathrm{m\,s^{-1}}$. Operating with a reduced switching frequency of $1\,\mathrm{kHz}$, the temperature can be kept even with lower fan speeds.

REFERENCES

[1] A. Lesnicar and R. Marquardt, "An innovative modular multilevel converter topology suitable for a wide power range," vol. 3, Bologna, Italy: IEEE, 2003, 6 pp.

[2] M. Glinka and R. Marquardt, "A new ac/ac multilevel converter family," *IEEE Transactions on Industrial Electronics*, vol. 52, pp. 662–669, 3 2005.

[3] W. Kawamura, M. Hagiwara, and H. Akagi, "A broad range of frequency control for the modular multilevel cascade converter based on triple-star bridge-cells (mmcc-tsbc)," Denver, CO, USA: IEEE, 2013, pp. 4014–4021.

[4] P. K. Steimer, O. Senturk, S. Aubert, and S. Linder, "Converter-fed synchronous machine for pumped hydro storage plants," Pittsburgh, PA, USA: IEEE, 2014, pp. 4561–4567.

[5] A. Christe, A. Faulstich, M. Vasiladiotis, and P. Steinmann, "World's first fully-rated direct ac/ac mmc for variable-speed pumped-storage hydropower plants," *IEEE Transactions on Industrial Electronics*, vol. PP, pp. 1–10, 99 2022.

[6] "Sinamics sh150 for special requirements," Siemens. (2023), [Online]. Available: https://new.siemens.com/global/en/products/drives/sinamics/medium-voltage-converters/sinamics-sh150.html.

[7] "M2l series medium voltage variable frequency drive," Benshaw. (2019), [Online]. Available: https://benshaw.com/wp-content/uploads/2020/01/benshaw-m2l-3000-brochure.pdf.

[8] "Mm7 modular multilevel converter," General Electric. (2021), [Online]. Available: https : / / www . gepowerconversion . com / sites / default / files / GEA34256_Modular % 20Multilevel % 20Converter_FLY_en_20210322.pdf.

[9] M. Vasiladiotis, R. Baumann, C. Häderli, and J. Steinke, "Igct-based direct ac/ac modular multilevel converters for pumped hydro storage plants," Portland, OR, USA: IEEE, 2018, pp. 4837–4844.

[10] J. Pan, Z. Ke, M. A. Sabbagh, *et al.*, "7-kv 1-mva sic-based modular multilevel converter prototype for medium-voltage electric machine drives," *IEEE Transactions on Power Electronics*, vol. 35, pp. 10 137–10 149, 10 2020.

[11] J. Yu, R. Burgos, N. R. Mehrabadi, and D. Boroyevich, "Design of a sic-based modular multilevel converter for medium voltage dc distriution system," Tampa, FL, USA: IEEE, 2017, pp. 467–473.

[12] B. Wang, L. Wang, S. Wu, *et al.*, "An evaluation on thermal performance improvements for sic power module integrated with vapor chamber in mmc," *IEEE Journal of Emerging and Selected Topics in Power Electronics*, vol. 10, pp. 5214–5225, 5 2022.

[13] H. Li, K. Potty, Z. Ke, *et al.*, "Hardware design of a 1.7 kv sic mosfet based mmc for medium voltage motor drives," San Antonio, TX, USA: IEEE, 2018, pp. 1649–1655.

[14] X. Feng, R. Kotecha, S. Narumanchi, *et al.*, "Multiscale electrothermal design of a modular multilevel converter for grid-tied applications," Vancouver, BC, Canada: IEEE, 2021, pp. 5657–5664.

[15] Y. Zhang, H. Wang, Z. Wang, and F. Blaabjerg, "System-level thermal modeling of a modular multilevel converter," New Orleans, LA, USA: IEEE, 2020, pp. 2766–2771.

[16] B. Li, S. Zhou, D. Xu, S. J. Finney, and B. W. Williams, "A hybrid modular multilevel converter for medium-voltage variable-speed motor drives," *IEEE Transactions on Power Electronics*, vol. 32, pp. 4619–4630, 6 2017.

[17] G. Konstantinou, S. Ceballos, I. Gabiola, J. Pou, B. Karanayil, and V. G. Agelidis, "Flexible prototype of modular multilevel converters for experimental verification of dc transmission and multiterminal systems," Singapore: IEEE, 2017, pp. 1–6.

[18] S. Mocevic, J. Yu, B. Fan, *et al.*, "High power density 10 kv sic mosfet-based modular, scalable converter for medium voltage applications," Houston, TX, USA: IEEE, 2022, pp. 422–429.

[19] M. Utvic, I. P. Lobos, and D. Dujic, "Low voltage modular multilevel converter submodule for medium voltage applications," Nuremberg, Germany: VDE, 2019, pp. 1–8.

[20] M. V. Soares and Y. R. de Novaes, "Mmc based hybrid switched capacitor dc-dc converter," *IEEE Open Journal of Power Electronics*, vol. 3, pp. 142–152, 2022.

[21] M. Glinka, "Prototype of multiphase modular-multilevel-converter with 2 mw power rating and 17-level-output-voltage," vol. 4, Aachen, Germany: IEEE, 2004, 2572–2576 Vol.4.

[22] F. Gao, Z. Li, P. Wang, *et al.*, "Prototype of smart energy router for distribution dc grid," Geneva, Switzerland: IEEE, 2015, pp. 1–9.

[23] P. Bontemps, S. Milovanovic, and D. Dujic, "Distributed real-time model of the m3c for hil systems using small-scale simulators," *IEEE Open Journal of Power Electronics*, vol. 2, pp. 603–613, 2021.

[24] A. Christe, E. Coulinge, and D. Dujic, "Insulation coordination for a modular multilevel converter prototype," Karlsruhe, Germany: IEEE, 2016, pp. 1–9.